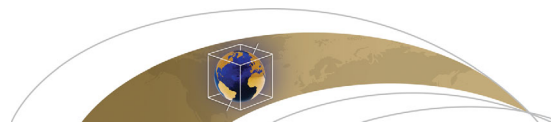




Title	Hydrogeological responses to incoming materials at the erosional subduction margin, offshore Osa Peninsula, Costa Rica
Author(s)	Kameda, Jun; Harris, Robert N.; Shimizu, Mayuko; Ujiie, Kohtaro; Tsutsumi, Akito; Ikehara, Minoru; Uno, Masaaki; Yamaguchi, Asuka; Hamada, Yohei; Namiki, Yuka; Kimura, Gaku
Citation	Geochemistry geophysics geosystems, 16(8), 2725-2742 <a href="https://doi.org/10.1002/2015GC005837">https://doi.org/10.1002/2015GC005837</a>
Issue Date	2015-09
Doc URL	<a href="http://hdl.handle.net/2115/60588">http://hdl.handle.net/2115/60588</a>
Type	article
File Information	Kameda_et_al-2015-Geochemistry,_Geophysics,_Geosystems.pdf



[Instructions for use](#)



## RESEARCH ARTICLE

10.1002/2015GC005837

## Special Section:

Subduction processes in Central America with an emphasis on CRISP results

## Key Points:

- Incoming material compositions at the Costa Rica margin were examined by XRD
- The sediment and basement contain abundant hydrous smectite and opal
- Diagenetic reactions significantly affect fluid circulation at this margin

## Correspondence to:

J. Kameda,  
kameda@mail.sci.hokudai.ac.jp

## Citation:

Kameda, J., et al. (2015), Hydrogeological responses to incoming materials at the erosional subduction margin, offshore Osa Peninsula, Costa Rica, *Geochem. Geophys. Geosyst.*, 16, 2725–2742, doi:10.1002/2015GC005837.

Received 1 APR 2015

Accepted 28 JUL 2015

Accepted article online 1 AUG 2015

Published online 21 AUG 2015

## Hydrogeological responses to incoming materials at the erosional subduction margin, offshore Osa Peninsula, Costa Rica

Jun Kameda<sup>1</sup>, Robert N. Harris<sup>2</sup>, Mayuko Shimizu<sup>3</sup>, Kohtaro Ujiie<sup>4</sup>, Akito Tsutsumi<sup>5</sup>, Minoru Ikehara<sup>6</sup>, Masaaki Uno<sup>7</sup>, Asuka Yamaguchi<sup>8</sup>, Yohei Hamada<sup>9</sup>, Yuka Namiki<sup>5</sup>, and Gaku Kimura<sup>10</sup>

<sup>1</sup>Department of Natural History Sciences, Graduate School of Science, Hokkaido University, Sapporo, Japan, <sup>2</sup>College of Earth, Oceanic and Atmospheric Sciences, Oregon State University, Corvallis, Oregon, USA, <sup>3</sup>Neotectonics Research Group, Japan Atomic Energy Agency, Gifu, Japan, <sup>4</sup>Doctoral Program in Earth Evolution Sciences, Graduate School of Life and Environmental Sciences, University of Tsukuba, Tsukuba, Japan, <sup>5</sup>Division of Earth and Planetary Sciences, Graduate School of Science, Kyoto University, Kyoto, Japan, <sup>6</sup>Center for Advanced Marine Core Research, Kochi University, Kochi, Japan, <sup>7</sup>Graduate School of Environmental Studies, Tohoku University, Sendai, Japan, <sup>8</sup>Ocean Research Institute, University of Tokyo, Tokyo, Japan, <sup>9</sup>Institute for Research on Earth Evolution, Japan Agency for Marine-Earth Science and Technology, Yokohama, Japan, <sup>10</sup>Department of Earth and Planetary Science, Graduate School of Science, University of Tokyo, Tokyo, Japan

**Abstract** Bulk mineral assemblages of sediments and igneous basement rocks on the incoming Cocos Plate at the Costa Rica subduction zone are examined by X-ray diffraction analyses on core samples. These samples are from Integrated Ocean Drilling Program Expedition 334 reference Site U1381, ~ 5 km seaward of the trench. Drilling recovered approximately 100 m of sediment and 70 m of igneous oceanic basement. The sediment includes two lithologic units: hemipelagic clayey mud and siliceous to calcareous pelagic ooze. The hemipelagic unit is composed of clay minerals (~50 wt.%), quartz (~5 wt.%), plagioclase (~5 wt.%), calcite (~15 wt.%) and ~30 wt.% of amorphous materials, while the pelagic unit is mostly made up of biogenic amorphous silica (~50 wt.%) and calcite (~50 wt.%). The igneous basement rock consists of plagioclase (~50–60 wt.%), clinopyroxene (~>25 wt.%), and saponite (~15–40 wt.%). Saponite is more abundant in pillow basalt than in the massive section, reflecting the variable intensity of alteration. We estimate the total water influx of the sedimentary package is 6.9 m<sup>3</sup>/yr per m of trench length. Fluid expulsion models indicate that sediment compaction during shallow subduction causes the release of pore water while peak mineral dehydration occurs at temperatures of approximately ~100°C, 40–30 km landward of the trench. This region is landward of the observed updip extent of seismicity. We posit that in this region the presence of subducting bathymetric relief capped by velocity weakening nanofossil chalk is more important in influencing the updip extent of seismicity than the thermal regime.

### 1. Introduction

Fluids play a critical role in tectonics and material transfer at convergent plate margins and have a fundamental influence on a number of subduction zone processes such as seismicity, arc magmatism, and the element transfer between the ocean, crust, and the mantle [e.g., Peacock, 1990; Kastner et al., 1991; Moore and Vrolijk, 1992; Wallace, 2005; Hacker, 2008; Saffer and Tobin, 2011; Kastner et al., 2014]. Most water entering subduction zones is initially trapped in sediment pores, but pore collapse due to tectonic loading within <~3–4 km of burial causes rapid dewatering [Bray and Karig, 1985; Moore and Vrolijk, 1992]. Subsequent dewatering occurs through dehydration of hydrous minerals such as smectite and biogenic opal. The progress of smectite-illite conversion and biogenic opal-quartz conversion reactions is governed by reaction kinetics, and in general continue to temperatures as high as ~150°C [Spinelli and Saffer, 2004; Saffer et al., 2008]. At greater temperatures, the completion of these reactions dries the system and is thought to lead to unstable behavior of the deeper plate boundary [Moore and Saffer, 2001].

The Costa Rica Seismogenesis Project (CRISP) offshore the Osa Peninsula, was undertaken to better understand erosional convergent margins and the role of fluids [Vannucchi et al., 2012]. In this study, we use X-ray diffraction (XRD) to quantify the mineral composition of material recovered at Site U1381, the sedimentary

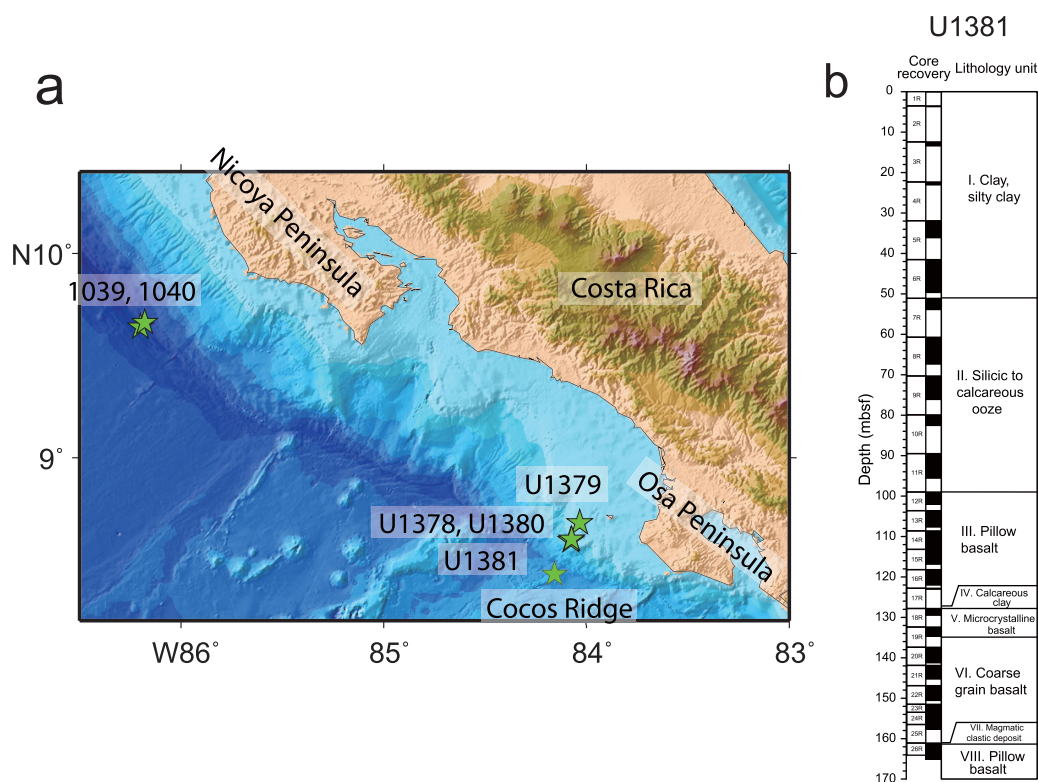


**Figure 1.** (a) Location of CRISP transect along the Middle America Trench. U1381 site 5 km seaward from the trench axis. Seismic lines CRP1600 and BGR99-15 for 2-D thermal modeling by Harris *et al.* [2010] are also shown. (b) Lithostratigraphy of the upper Cocos Plate at the U1381A site.

reference site seaward of the Middle America Trench. We pay particular attention to the hydrous component and use this information to estimate fluid flux into this margin, address how fluids are released from the incoming materials, and then provide some insights into plate boundary hydrologic and seismogenic processes at the CRISP transect.

## 2. Geological Background and IODP Site U1381A

Along the Middle America Trench, the Cocos Plate subducts to the northeast beneath the Caribbean Plate at approximately 85 mm/yr [DeMets, 2001, Figure 1a]. Drilling and seismic surveys along the margin suggest active and long-term tectonic erosion [Ranero and von Huene, 2000; Ranero *et al.*, 2000; Vannucchi *et al.*, 2001, 2003, 2004]. Active fluid venting documented by ubiquitous mud mounds and seepages is widespread along strike [Sahling *et al.*, 2008; Kluesner *et al.*, 2013]. Several geochemical signatures (e.g., low salinity, isotopic features and entrainment of thermogenic methane) indicate that discharged fluids originate from dehydration reactions at temperatures between 85° and 150°C [Hensen *et al.*, 2004; Schmidt *et al.*, 2005].

The CRISP drilling transect, northwest of the Osa Peninsula, is located on the northern flank of the Cocos Ridge where the seismogenic zone extends updip to shallow depths (Figure 1). The Cocos Ridge stands approximately 2.5 km above the regional seafloor and was formed as the plate passed over the Galapagos hotspot. The onset of the Cocos Ridge subduction is controversial and ranges from ~1 Ma to ~8 Ma [Hey, 1977; Lonsdale and Klitgord, 1978; Sutter, 1985]. The present-day subduction of the Cocos Ridge is thought to affect several aspects of regional tectonic features such as concavity of trench axis [Vannucchi *et al.*, 2013], shallow seismicity, 5–10 km below the seafloor, 25–30 km landward of the deformation front [DeShon *et al.*, 2003; Arroyo *et al.*, 2014], complicated earthquake rupture processes [Bilek *et al.*, 2003], and higher plate coupling and stress state as indicated by on-land GPS data [Dixon, 2003].

IODP Expedition 334 cored four sites along the CRISP transect [Vannucchi *et al.*, 2012]. Three of these sites are located on the trench slope of the forearc prism and one site (U1381A) on the Cocos plate seaward of

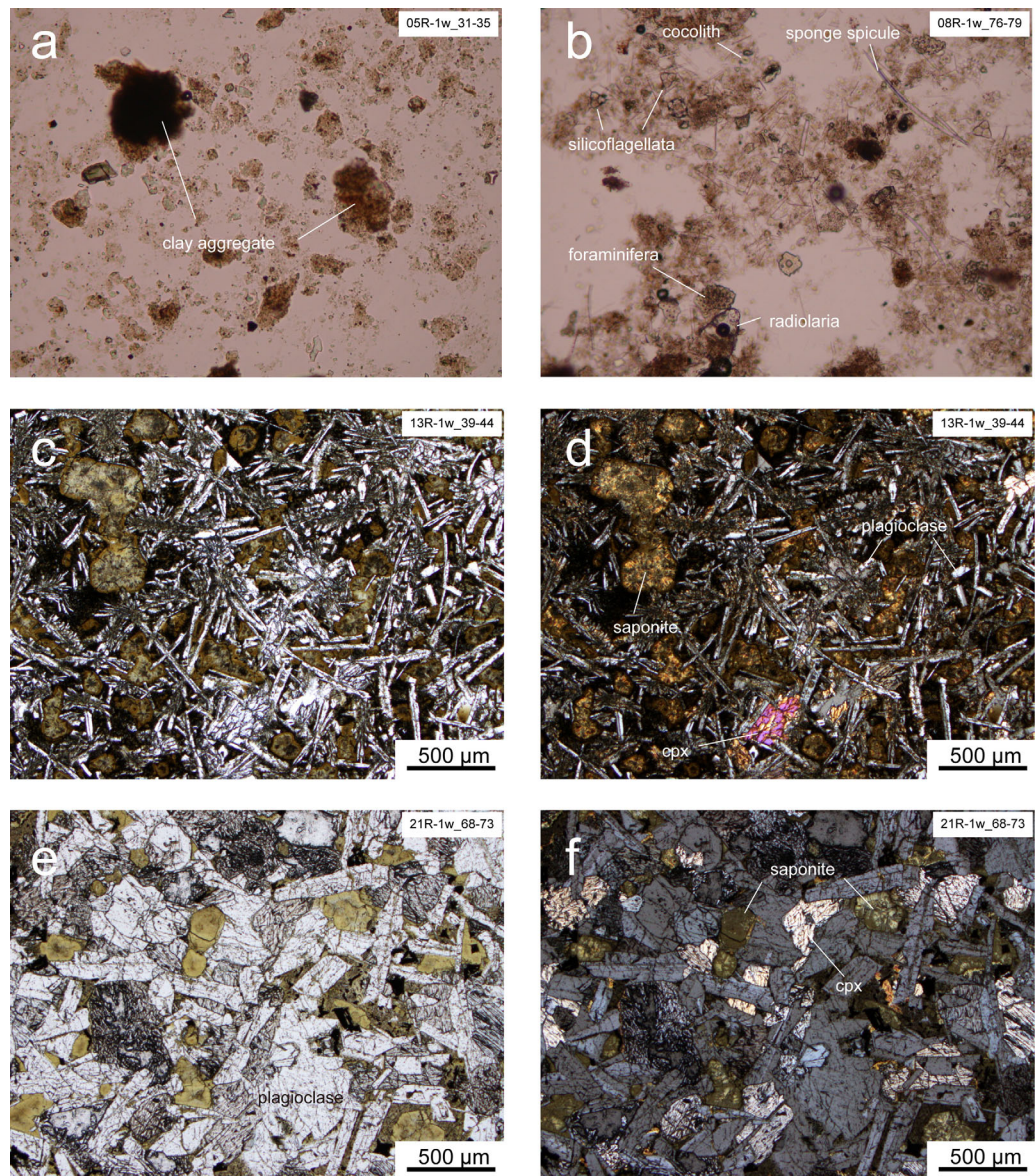


**Figure 2.** Typical appearance of (a) hemipelagic mud (Unit I) and (b) pelagic ooze (Unit II) under optical microscope. Microtexture of pillow basalt under (c) nonpolarized and (d) polarized light. Vesicles are filled with authigenic clay (saponite). Microtexture of massive basalt under (e) nonpolarized and (f) polarized light. Saponite typically occurs as replacement possibly after olivine. cpx=clinopyroxene.

the trench (Figure 1a) [Vannucchi *et al.*, 2012]. Drilling at U1381A (8°25.7150'N, 84° 9.4690'W) recovered approximately 100 m of sedimentary cover and 70 m of oceanic basement. Shipboard analysis identified two lithologic units in the sediment section (Figure 1b). Unit I consists of ~50 m of hemipelagic mud mainly consisting of light greenish-gray clayey sediment (Figure 2a) that contains several tephra layers (2–4 cm thick). Unit II consists of ~50 m thick of silicic to calcareous pelagic ooze (Figure 1b) that is dark grayish to yellowish brown, soft to hardened clay with abundant intercalated tephra layers. Unit II also contains abundant biogenic components such as spicules, diatoms, radiolarians, and calcareous nannofossils (Figure 2b). The nannofossil assemblage suggests that the deposition age ranges from lower Pleistocene (Unit 1) to middle Miocene (Unit II) [Vannucchi *et al.*, 2012].

Shipboard core description of the igneous basement divided the section into six units (Unit III-VIII; Figure 1b). Unit III is plagioclase phyric to glomerophyric pillow basalts (Figures 2c and 2d) with a set of chilled margins, which is followed with a thin calcareous claystone layer (Unit IV). Unit V is composed of an aphyric to moderately plagioclase phyric pillow basalts. Unit VI consists of coarser grained aphyric to moderately

plagioclase phyric massive basalts (Figures 2d and 2e). The bottom of Unit VI is a clastic magmatic horizon, mainly composed of basalt- and plagioclase-derived clasts in a fine-grained to microcrystalline matrix (Unit VII). Another plagioclase phyric pillow basalt occurs in the bottom section (Unit VIII). Ubiquitous vesicles are observed throughout the basalt (up to 20 vol.%), but they are commonly filled with authigenic clay minerals (Figures 2c and 2d).

### 3. Laboratory Methods

Relative mineral proportions in bulk samples were examined by XRD and processed using newly developed normalization factors for CRISP samples (section 4). Powder XRD patterns were recorded using a Rigaku Rint-Ultima 2100 with one-dimensional X-ray detector (D/teX Ultra, Rigaku) at 40 kV and 30 mA, with 0.5° and 10 mm divergence slits and a 8 mm anti-scattering slit, at a scan rate of 1° per min at 0.02° step in  $2\theta$ . Diagnostic reflections from individual mineral species were processed (linear background subtraction, counting of integrated peak intensity) using standard Rigaku peak analysis software. In determining absolute abundance of the constituent minerals including noncrystalline materials, calcite content was independently measured by Coulometric analysis. Based on results from the Coulometry, the absolute content of other crystalline phases (i.e., clay minerals, quartz and plagioclase) was determined by XRD. The amorphous content was then calculated by subtracting total abundance of crystalline phases from 100%.

For the clay mineral analysis, bulk powders were gently crushed, dispersed ultrasonically in distilled water, and the clay fraction ( $<2.0\ \mu\text{m}$ ) was separated by centrifugation. Clay suspensions were washed three times in 1M  $\text{CaCl}_2$  solutions to prepare Ca-saturated specimens (more than 6 h immersion for each treatment), and dropped onto glass slides to prepare oriented mounts by air-drying in an oven at 60°C (herein referred to as the "AD" (air drying) state). These mounts were subsequently saturated with ethylene-glycol vapor at 60°C for more than 5 h ("EG" state). XRD patterns for the oriented mounts were recorded using a Rigaku Rint-2500 with monochromatized  $\text{CuK}\alpha$  radiation at 40 kV and 200 mA, with 0.5° divergence and anti-scattering slits, and a 0.3 mm receiving slit over 2–35°  $2\theta$  range. The expandability of smectite (%S in illite-smectite mixed layer (I-S)) was estimated from the saddle/peak ratio of I-S 001 reflection in EG-XRD pattern, using a working curve of *Inoue et al.* [1989]. We also applied a weighting factor proposed by *Biscaye* [1965] to EG-XRD patterns in order to estimate relative proportions of clay phases in clay fraction samples (1× for smectite, 2× for kaolinite and chlorite and 4× for illite).

The water content in biogenic silica was measured with thermogravimetric analysis combined with differential thermal analysis (TG-DTA) at a heating rate of 10°C per min. For purification of biogenic silica, pelagic samples were immersed in 0.5N HCl solution to digest tests of biogenic calcite before TG-DTA analysis.

### 4. Normalization Factors for Bulk XRD

For quantitative analysis of XRD patterns, we developed two normalization factors for sediment and smectite-bearing basalt samples in the recovered cores. From preliminary scans, we prepared 12 standard mixtures composed of montmorillonite (SWy-2; The Clay Minerals Society (CMS)), kaolinite (KGa-2; CMS), illite (IMt-2; CMS), plagioclase (Ca-albite; Nichica Inc.), quartz and calcite (reagents from Kanto Chemical Co., Inc.) for sediment standards, and 6 mixtures composed of saponite (JCSS-3501; The Clay Science Society of Japan), plagioclase (anorthite; Nichica Inc.), and pyroxene (diopside; Nichica Inc.) for altered basalt standards, with variable wt.% combinations (Table 1). Each mineral standard was preheated in an oven at 60°C for 3 h, and was blended in an agate mortar. XRD patterns for the standard mixtures were recorded in the same measurement setting as that for bulk sample measurement (section 3).

In addition to correlations between the intensity of diagnostic reflection and its actual abundance, the peak intensity from a given mineral is also influenced by other mineral species in the same sample [*Fisher and Underwood*, 1995]. To determine the appropriate coefficient for correcting this matrix effect, an optimal normalization factor is derived by the least squares method for each series of the standard mixtures (Table 2). The comparison between the calculated and actual abundance of the standard mixtures suggests that potential errors in this procedure are approximately 10 wt.% (Table 1 and Figure 3).

**Table 1.** Standard Mixtures and Corresponding Calculated Abundance

Standard Sample Sediment	wt% (Weighed)				wt% (Calculated)			
	Clay	Quartz	Plagioclase	Calcite	Clay	Quartz	Plagioclase	Calcite
1	4.8	10.2	15.0	69.9	5.1	10.2	18.2	62.0
2	9.6	15.5	69.9	5.1	10.2	15.1	71.9	2.7
3	14.4	70.6	5.0	10.0	15.5	71.7	3.2	9.3
4	66.8	8.1	10.0	15.0	67.0	9.5	9.0	15.7
5	23.9	26.1	25.0	25.0	25.2	25.7	22.9	26.1
6	38.3	41.7	10.0	10.0	37.2	38.5	6.8	9.6
7	9.6	10.5	40.0	40.0	10.1	11.4	31.8	48.7
8	47.8	37.1	5.0	10.0	47.0	35.2	6.3	10.8
9	9.6	30.4	10.0	49.9	9.1	30.4	15.7	50.8
10	76.4	13.5	5.0	5.0	76.7	14.8	7.5	3.5
11	9.6	50.4	30.0	10.0	8.9	52.2	31.8	10.5
12	4.9	10.2	49.9	34.9	3.6	9.4	49.3	34.8

Standard Sample Basalt	wt% (Weighed)			wt% (Calculated)		
	Saponite	Plagioclase	Pyroxene	Saponite	Plagioclase	Pyroxene
1	5	10	85	8.2	8.9	82.1
2	10	85	5	11.9	84.7	4.1
3	85	5	10	87.2	3.0	11.2
4	33	33	33	28.2	29.4	38.9
5	20	15	65	18.5	18.2	65.7
6	65	20	15	63.7	23.6	11.1

## 5. Analytic Results

### 5.1. Mineral Composition of Sediments

Typical examples of bulk XRD for hemipelagic mud (03R-1w-33–36cm), pelagic ooze (09R-1w-28–30cm) and an intermediate horizon (07R-1w-53–57cm) are shown in Figure 4. The hemipelagic mud contains smectite, kaolinite, quartz, plagioclase and calcite. In contrast, the pelagic ooze contains only calcite as a crystalline phase, but the XRD pattern shows a broad intensity high at  $\sim 22^\circ 2\theta$ , attributed to biogenic amorphous silica. The XRD pattern of core 07R-1w (57–53 cm), near the bottom of Unit I, also contains reflections from smectite, plagioclase and quartz, but the peak intensities are weaker than those of the hemipelagic mud. Sediment samples also commonly show a halite peak as an evaporite of interstitial seawater. The results of the quantitative bulk analyses are plotted next to the lithostratigraphic column (Figure 5 and Table 3). The quantitative bulk analyses demonstrate a mineralogical contrast between Units I and II consistent with their depositional settings (Figure 5). The hemipelagic unit contains  $\sim 50$  wt.% of clays,  $\sim 5$  wt.% of quartz and plagioclase,  $> 15$  wt.% of calcite, and  $\sim 30$  wt.% of amorphous materials. The pelagic unit lacks detrital materials, and is mostly composed of amorphous silica ( $\sim 50$  wt.%) and calcite ( $\sim 50$  wt.%) of biogenic origin (Figure 2b).

Clay-fraction XRD of hemipelagic mud shows intensity peaks corresponding to smectite, weaker kaolinite and zeolite reflections, and a trace peak corresponding to illite (Figure 6). Smectite has high

**Table 2.** Normalization Factors for Sediment and Basalt

Indicator Mineral Sediment	Target Mineral Sediment			
	Clay	Quartz	Plagioclase	Calcite
Clay	$2.00 \times 10^{-2}$	$6.40 \times 10^{-4}$	$9.69 \times 10^{-4}$	$-6.60 \times 10^{-4}$
Quartz	$7.35 \times 10^{-5}$	$8.42 \times 10^{-4}$	$-4.50 \times 10^{-5}$	$-1.10 \times 10^{-5}$
Plagioclase	$-4.60 \times 10^{-5}$	$-3.20 \times 10^{-5}$	$8.06 \times 10^{-4}$	$-4.00 \times 10^{-5}$
Calcite	$5.58 \times 10^{-5}$	$1.05 \times 10^{-4}$	$2.18 \times 10^{-4}$	$1.50 \times 10^{-3}$
Indicator Mineral Basalt	Target Mineral Basalt			
	Saponite	Plagioclase	Pyroxene	
Saponite	$3.43 \times 10^{-3}$	$-5.60 \times 10^{-5}$	$-3.30 \times 10^{-4}$	
Plagioclase	$3.62 \times 10^{-4}$	$4.45 \times 10^{-3}$	$-5.00 \times 10^{-5}$	
Pyroxene	$4.80 \times 10^{-4}$	$1.29 \times 10^{-4}$	$8.08 \times 10^{-3}$	

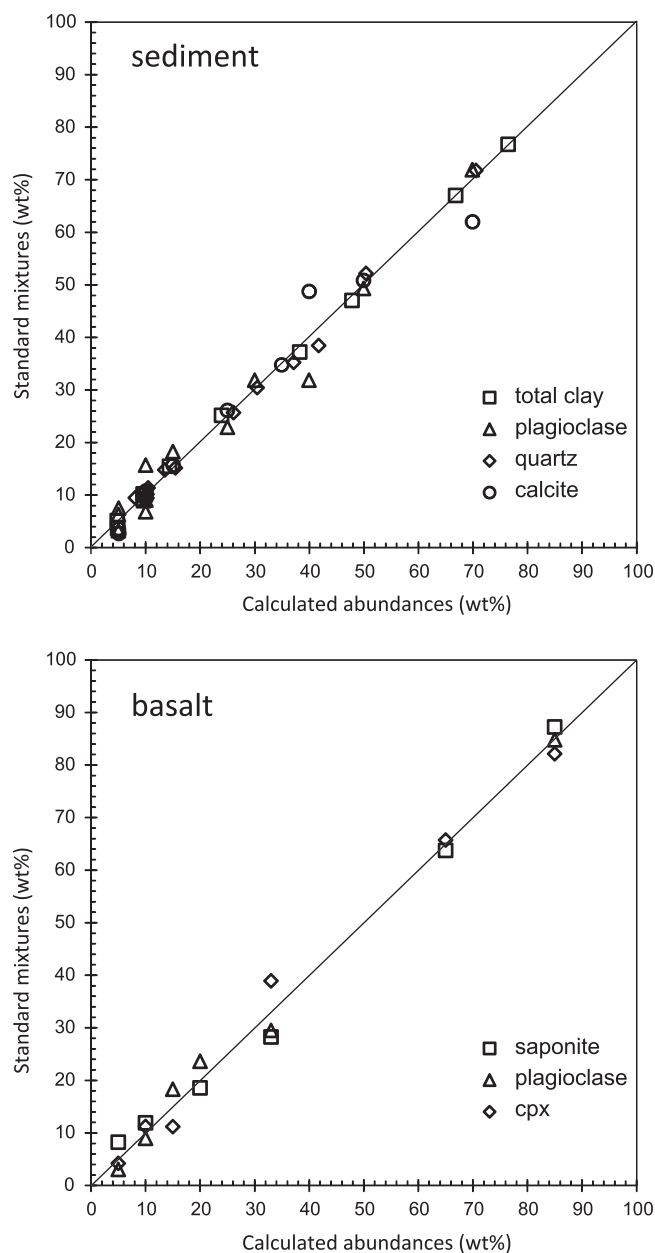


**Figure 3.** Weight populations in standard mixtures of (a) sediment and (b) basalt samples against calculated abundances by quantitative analyses (see the text for detailed explanation).

layer, and three-layer hydration). The 060 diffraction angle suggests that smectite is trioctahedral saponite (Figure 7b). The occurrence of saponite in these samples was also confirmed by electron probe microanalysis (M. Uno, 2014, unpublished data).

**5.3. Water Content in Biogenic Amorphous Silica**

The pelagic unit contains a variety of biogenic remains made up of amorphous silica (e.g., diatom and sponge spicule) and calcite (e.g., foraminifera and cocolith) (Figure 2b). Of these tests, amorphous silica (opal-A) is important because it initially contains substantial amounts of bound water, which is successively released during subsequent diagenetic transformation into quartz. TG-DTA analysis showed that the biogenic amorphous silica contains approximately 12 wt.% of water (Figure 10). This result is consistent with the previous estimates for several species of opal [Kastner, 1981] and sponge spicules (10–15 wt.%) [Sandford, 2003], but is slightly smaller than in the diatom-rich silica sinters (15–20 wt.%)

expandability (~85 %S in I-S), and has a 060 diffraction angle at 61.8° 2θ, suggesting a dioctahedral member of smectite such as montmorillonite (Figure 7a). The relative proportions of clay phases in the clay fraction samples is 92 wt.% of smectite, 8 wt.% of kaolinite and <1% of illite. This composition is nearly constant over the hemipelagic unit.

**5.2. Mineral Composition of Altered Basalt**

Bulk XRD patterns for upper pillow basalt (13R-1w-39–44cm), massive basalt (20R-1w-104–108cm), and lower pillow basalt at the bottom (26R-1w-130–135cm) are shown in Figure 8. Mineral assemblages are as a whole smectite, plagioclase (anorthite) and clinopyroxene, but relative peak intensities suggest variable proportions of these phases among the samples. Quantitative analysis reveals that saponite content is relatively higher in the pillow basalt than in the massive section at an interval of 130–160 m below sea-floor (mbsf) (Figure 5 and Table 4). There is a weak inverse correlation between the saponite and pyroxene contents. Saponite content is highest in the lower pillow basalt, suggesting that alteration has advanced more than in the uppermost section (Figure 5).

Clay-fraction XRD patterns show a strong peak of smectite 001, and its nearly symmetric shape in EG state suggests a highly expandable discrete smectite (Figure 9). Its relatively complex shape in the AD-XRD patterns reflects variable hydration states of smectite interlayer (i.e., one-layer, two-

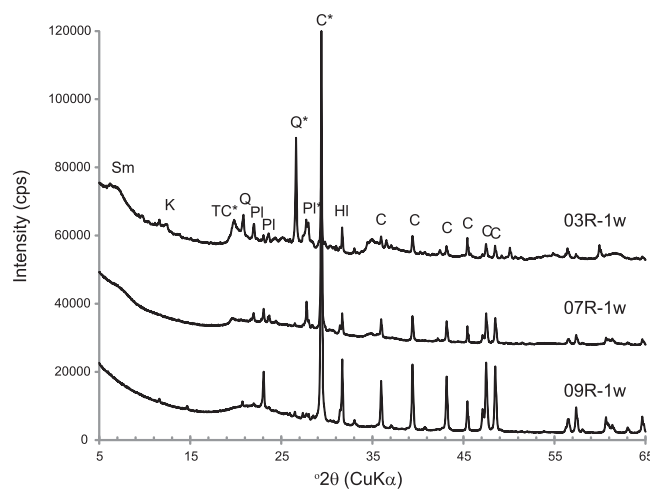


**Figure 4.** Bulk powder XRD patterns for hemipelagic mud (03R-1w), pelagic ooze (09R-1w) and sample from an intermediate horizon between the two units (07R-1w). Sm=smectite; K=kaolinite; TC=total clay; Pl=plagioclase; C=calcite; H=halite. Peaks marked by stars are reflections for quantitative analyses.

[Garcia-Valles *et al.*, 2008]. Given the general density of sponge spicules and opal (~2.1 g/cm<sup>3</sup>) [Sandford, 2003], the volume content of water is approximately 24 vol.%.

## 6. Fluid Budget

### 6.1. Influx of Water at the CRISP Transect

We estimate the fluid budget along the CRISP transect based on our data. The porosity, mineral assemblage, thickness of input materials, and plate convergence rate control the fluid flux into the subduction zone. The average porosity of the 50 m hemipelagic unit is 75% [Vannucchi *et al.*, 2012]. Given the plate convergence rate of 8.5 cm/yr, the hemipelagic section

carries 3.2 m<sup>3</sup>/yr of pore water per m of along strike trench length (Table 5). The solid fraction contains on average ~50 wt.% of smectite and ~30 wt.% of amorphous biogenic silica (Figure 5). These weight contents can be converted to ~48% and ~33% by volume, respectively, using an average density of constituent minerals of smectite (~2.4 g/cm<sup>3</sup>), sponge spicule or opal (~2.1 g/cm<sup>3</sup>), quartz (2.6 g/cm<sup>3</sup>), plagioclase (2.7 g/cm<sup>3</sup>) and calcite (2.7 g/cm<sup>3</sup>). The water content in smectite and biogenic silica is ~40 vol.% (two-layer hydration) [Bird, 1984; Fitts and Brown, 1999] and ~24 vol.% (see 5.3 section), respectively. Accordingly, the solid fraction delivers 0.28 m<sup>2</sup>/yr of fluid (5.6 × 10<sup>-3</sup> m/yr per unit thickness of solid; Table 5).

Using the same approach, the pelagic ooze is estimated to deliver 3.3 m<sup>3</sup>/yr per meter of trench length of pore fluid based on an average porosity of 78%. The sediment is composed of approximately 59 vol.% (53 wt.%) of biogenic silica. The solid fraction accounts for 0.13 m<sup>2</sup>/yr of water influx (2.6 × 10<sup>-3</sup> m/yr per unit thickness of solid; Table 5). The total water influx rate associated with pelagic unit is 3.4 m<sup>2</sup>/yr, such that the total water influx of the sedimentary package is 6.9 m<sup>2</sup>/yr.

In the igneous basement, hydrous saponite is widespread throughout the cored interval. The average content of saponite is approximately ~25 wt.% (Figure 5). Assuming the same density for saponite and bulk grain of basalt, and 5% porosity of the rock [Cann and von Herzen, 1983], the basalt carries 0.3 m<sup>2</sup>/yr of pore water, as well as 0.54 m<sup>2</sup>/yr of saponite-bound water (Table 5). It is uncertain how deep the alteration zone proceeds below the drilling hole at the CRISP margin, and thus this estimate is a minimum fluid influx rate due to the basalt section.

### 6.2. Dewatering From the Subducting Cocos Plate and Upward Fluid Migration

Once the incoming materials start subducting, both sediment compaction and later mineral dehydration reactions cause successive expulsion of water from the subducting oceanic plate. These dewatering processes affect interplate hydrology and may affect seismicity. Here we model dewatering following the approach of Spinelli *et al.* [2006] for silica diagenesis formulated by Mizutani [1977] and for clay diagenesis by Pytte and Reynolds [1989].

We first consider compaction dewatering from each incoming sediment unit. Shipboard porosity data in the hemipelagic unit at U1381 [Vannucchi *et al.*, 2012], are not significantly different from those measured at Site 1039 offshore the Nicoya Peninsula [Shipboard Scientific Party, 1997a, 1997b, 1997c]. Porosity values in the pelagic unit at Site U1381 are higher than those at Site 1039 because there is less overburden, but the trend is similar. Our compaction curves for the two sedimentary units are follow those from Site 1039 where there is more data,

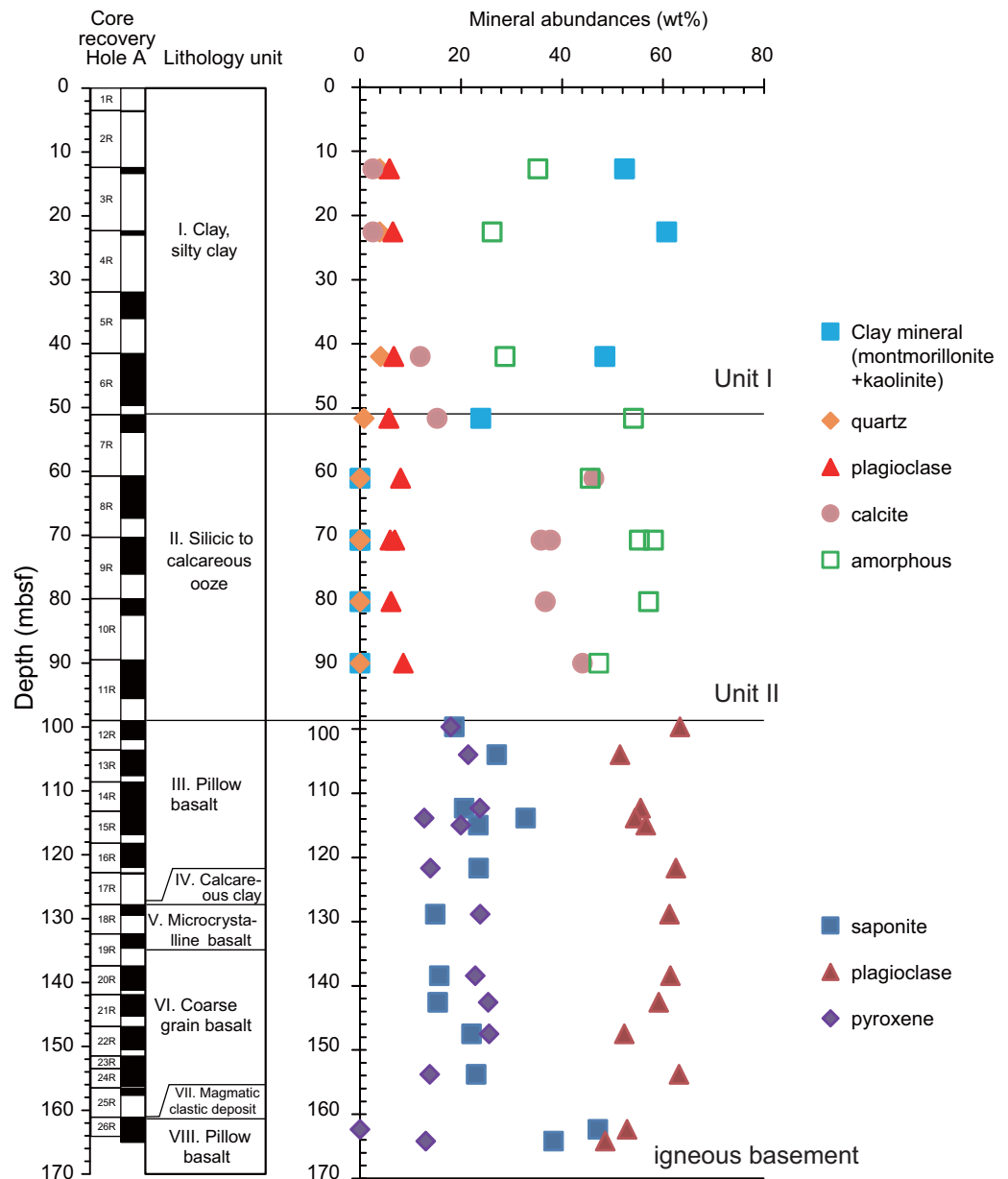


**Figure 5.** Mineral mode variation derived by combining quantitative XRD and Coulometry analyses. TC = total clay. Amorphous material in sediment sections is mostly biogenic silica (opal-A) based on smear slide observation.

$$\begin{aligned} \phi(z) &= 0.78 \exp(-0.58z) \quad \text{for unit I} \\ \phi(z) &= 0.81 \exp(-0.52z) \quad \text{for unit II} \end{aligned} \tag{1}$$

where  $\phi$  is porosity and  $z$  is depth (km) of sediment below the seafloor. We also assume that the above porosity-depth curves follow a generic subduction zone trend at deeper burial conditions [Bray and Karig, 1985];

$$\phi(z) = 0.16 \exp(-0.20z) \tag{2}$$

The dehydration source term,  $\Gamma$ , is calculated with respect to silica diagenesis (i.e., opal-A to quartz conversion) and clay diagenesis (i.e., smectite to illite conversion). For silica diagenesis, the initial amorphous phase (biogenic opal-A) is kinetically transformed into quartz through intermediate opal-CT. Following

**Table 3.** Results of Quantitative Analyses on Sediment Samples

Sample	mbsf	Unit	Integrated Peak Intensity				Wt% From Normalization Factor					Wt% From Coulometry	Wt% with Coulometry Results				
			Clay	Quartz	Plagioclase	Calcite	Clay	Quartz	Plagioclase	Calcite	Amorphous	Calcite	Clay	Quartz	Plagioclase	Calcite	Amorphous
3R-1w-33-36	12.73	I	2487	5224	3765	2983	52.40	3.88	5.86	2.60	35.26	6.92	139.6 <sup>a</sup>	10.3 <sup>a</sup>	15.6 <sup>a</sup>	6.9 <sup>a</sup>	-72.4 <sup>a</sup>
4R-1w-27-29	22.57	I	2719	5092	3846	2982	57.23	3.70	6.16	2.44	30.46	2.59	60.7	3.9	6.5	2.6	26.2
6R-1w-25-28	42	I	1961	4004	2906	7837	41.63	3.53	5.77	10.25	38.82	11.94	48.5	4.1	6.7	11.9	28.7
Average <sup>b</sup>		I											53.9 (5.1)	4.0 (0.1)	6.4 (0.4)	5.7 (4.4)	30.1 (3.8)
7R-1w-53-57	51.63	II	722	88	1848	6956	15.42	0.53	3.70	9.85	70.50	15.30	24.0	0.8	5.8	15.3	54.2
8R-1w-26-28	60.96	II	0	0	1310	25153	0.00	0.00	6.54	37.55	55.91	46.34	0.0	0.0	8.1	46.3	45.6
9R-1w-27-29	70.57	II	0	0	876	22031	0.00	0.00	5.51	32.90	61.59	35.88	0.0	0.0	6.0	35.9	58.1
9R-1w-28-30	70.58	II	0	0	1433	20886	0.00	0.00	5.71	31.17	63.12	37.74	0.0	0.0	6.9	37.7	55.4
10R-1w-28-30	80.18	II	0	0	887	22077	0.00	0.00	5.53	32.97	61.50	36.71	0.0	0.0	6.2	36.7	57.1
11R-1w-27-30	89.77	II	0	0	2194	24207	0.00	0.00	7.04	36.10	56.85	44.10	0.0	0.0	8.6	44.1	47.3
Average <sup>c</sup>		II											0.0 (0.0)	0.0 (0.0)	7.1 (1.0)	40.2 (4.2)	52.7 (5.2)

<sup>a</sup>Because of low abundance of calcite, errors in coulometry analysis can be amplified in the final results. Original wt% values from normalization factor are adopted for calculating as quantitative data of this sample.

<sup>b</sup>Averaged wt% values for Unit I are calculated by using original wt% values of the sample 3R-1w\_33-36 from normalization factor. Values in brackets are 1σ.

<sup>c</sup>Averaged wt% values for Unit II are calculated from five samples (8-11R) excluding 7R-1w\_53-57 because of its intermediate mineral composition between Unit I and Unit II. Values in brackets are 1σ.

Mizutani [1977], each step of the conversion reaction (i.e., opal-A to -CT and opal-CT to quartz) obeys the Arrhenius-type rate law, and is expressed in the following form:

$$\frac{\partial A}{\partial t} = -kA \tag{3}$$

where *A* is the mole fraction of reactant (opal-A and opal-CT), *t* is time, and *k* is the rate constant described as:

$$k = a \exp(-E/RT) \tag{4}$$

*a* is the frequency factor (23,700 yr<sup>-1</sup> for opal-A to -CT transition and 71,100 yr<sup>-1</sup> for opal-CT to quartz transition), *E* is activation energy (16 x 10<sup>3</sup> cal/mol for both reactions), *R* is gas constant and *T* is temperature. Water content in opal-A and opal-CT is 24 vol.% and 11 vol.%, respectively, which is released successively as reaction proceeds. For clay dehydration, we adopt the kinetic expression of Pytte and Reynolds [1989], which describes the smectite to illite conversion reaction as a change in %S (*S*) in I-S:

$$\frac{\partial S}{\partial t} = -A \exp\left(-\frac{E}{RT}\right) \left(\frac{[K^+]}{[Na^+]}\right)^n \tag{5}$$

where *A* is the frequency factor (5.2 x 10<sup>7</sup> s<sup>-1</sup>), *E* is the activation energy (1.38 x 10<sup>5</sup> J/mol), *n* is an exponent defining the reaction order with respect to *S* (*n*=5). Equilibrium between Albite and K-feldspar is assumed to control the activity ratio between K and Na in the reacting fluid [Pytte and Reynolds, 1989]. We adopted 85 %S in I-S for initial state of *S* (see section 5.1) and 20 vol.% of water in I-S.

Sediment temperatures are based on 2-D numerical models that fit observations of surface heat flow and heat flow estimated from bottom simulating reflectors along seismic line CRP-1600 equivalent to BGR99-7 [Harris et al., 2010]. We compare thermal models that differ in the value of the effective coefficient of friction. Our cool model corresponds to no frictional heating and our warm model corresponds to an effective coefficient of friction of 0.03. We show the temperature for both models that correspond to a depth of 50 m in the sediment (Figure 11a). Both models incorporate fluid flow along the subducting upper oceanic plate aquifer as developed by Spinelli and Wang [2009] and are cooler than those modeled by Spinelli et al. [2006] offshore the Nicoya Peninsula. The change in slope of the subduction thrust temperatures at a distance of ~8 km, corresponding to a depth of ~3.8 km shows the change from where modeled fluid flow is cooling the subduction thrust to where fluid is heating it. Figure 11a also shows the temperatures along the plate interface formulated by Ranero et al. [2008] from seismic line BGR99-15, just north of the CRISP drilling transect. For discussion we term this the hot model. Their temperatures are based on downward extrapolations of surface heat flow. We suspect these temperatures may be too high because the downward advection of

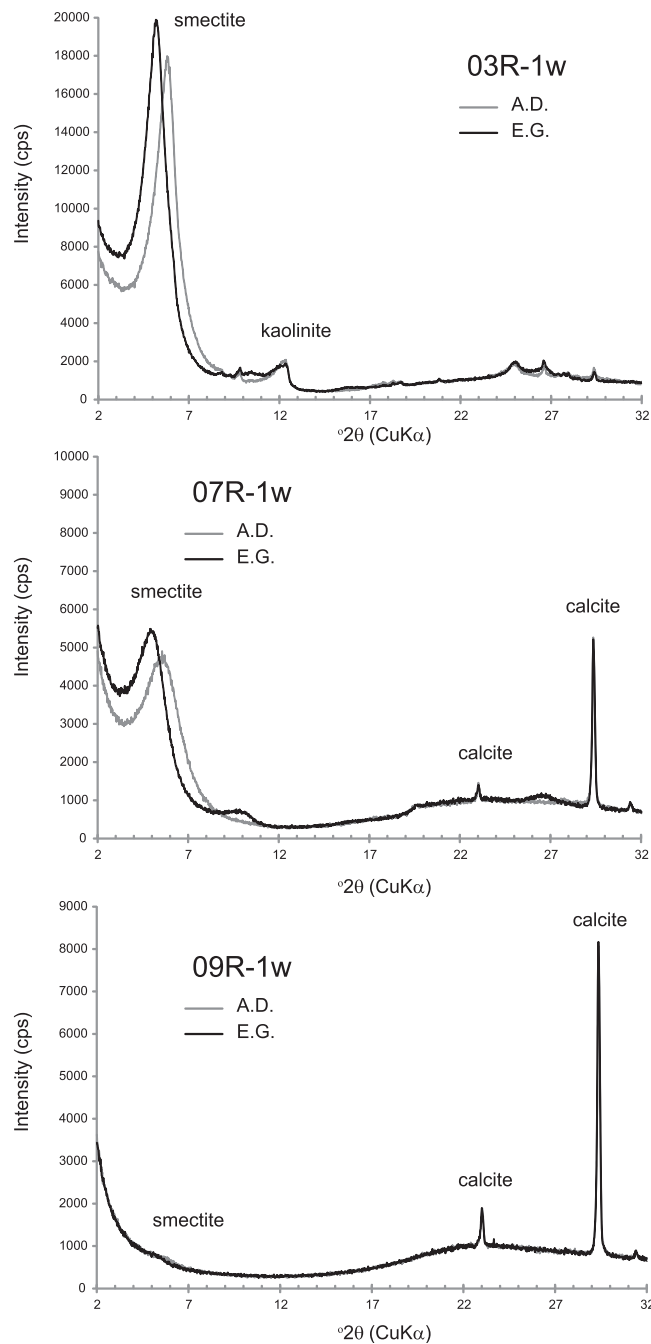


**Figure 6.** Clay-fraction XRD patterns (AD and EG states) for oriented mounts of hemipelagic clay (03R-1w), pelagic ooze (09R-1w) and sample from an intermediate horizon between the two units (07R-1w).

causes active fluid dehydration at approximately 15, 25 and 40 km landward from the trench for the hot, warm, and cool models, respectively (Figure 11c). Figure 11d shows total fluid release through compaction and mineral dehydration as a function of distance. These magnitudes are significantly less than those found offshore the Nicoya Peninsula [Spinelli et al., 2006] primarily due to the thinner incoming sediment here. Only the cool and warm models show regions where mineral dehydration significantly exceeds the compaction curve. These regions begin at distances of ~ 40 and 50 km landward of the trench for the cool and warm model, respectively.

Neuzil [1995] showed that overpressures are possible if the ratio of the hydraulic conductivity and path length is less than the source term,

heat with the slab is neglected [e.g., Molnar and England, 1995]. The warm and hot models agree to distances of about 6 km landward of the trench but then diverge.

Figure 11 shows how dewatering proceeds in the two sedimentary units. Compaction dewatering dominates near the trench, and gradually decreases with distance from the trench. The different diagenetic dehydration curves reflect the different thermal models. Relative to the cool model, frictional heating shifts peak dehydration to shallower depths. In the hemipelagic unit, silica diagenesis occurs with a pulse of dehydration at distances around ~25 and 40 km from the trench for the warm and cool models, respectively (Figure 11b). Both peaks correspond to temperatures of approximately 90°C. Further down dip at higher temperatures, clay diagenesis show maximum dehydration values at distances of approximately 35 and 55 km from the trench for the warm and cool models, respectively. These dehydration peaks correspond to temperatures of 110°C. Peak silica dehydration just reaches the compaction dewatering curves, whereas because of the deeper onset of clay dehydration, peak values exceed the compaction dewatering curve. The warmer temperatures associated with the hot model lead to peak dehydration of silica and clay at distances of approximately 13 and 16 km landward from the trench, respectively (Figure 11b). The rapid rise in temperatures narrow the region over which mineral bound water is released, such that the clay dehydration is largely completed at distances 30 km from the trench. Only the dehydration of clays in the warm and cool model significantly exceeds the fluid release from compaction. In the pelagic unit, silica diagenesis

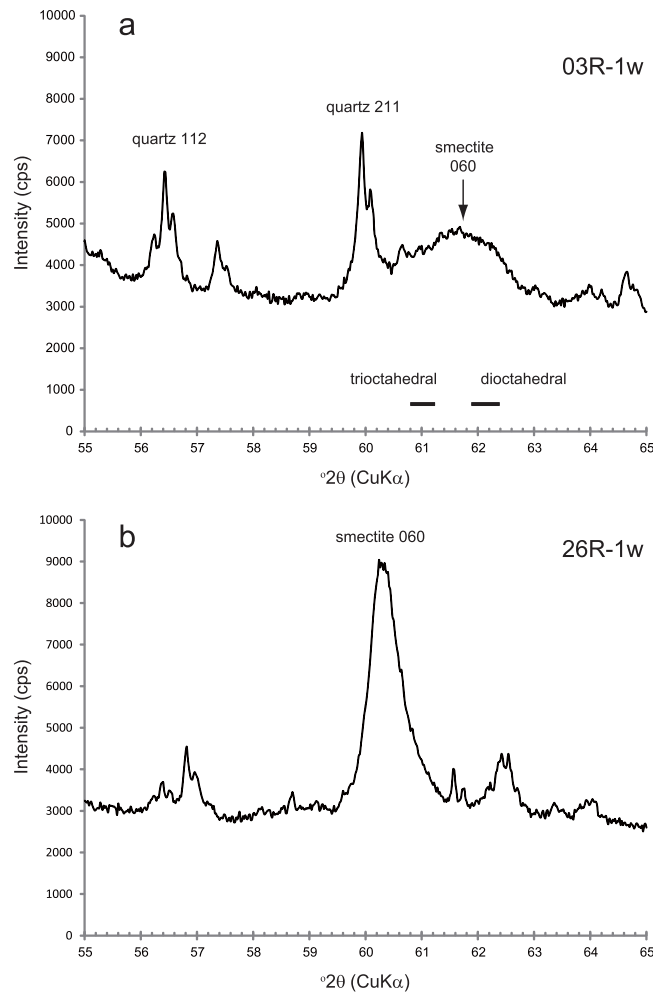


**Figure 7.** Smectite 006 reflection in bulk powder XRD patterns. (a) The peak in sediment sample locates close to typical d-spacings for dioctahedral smectite member (possibly montmorillonite), (b) while that in basalt sample is close to trioctahedral member (saponite).

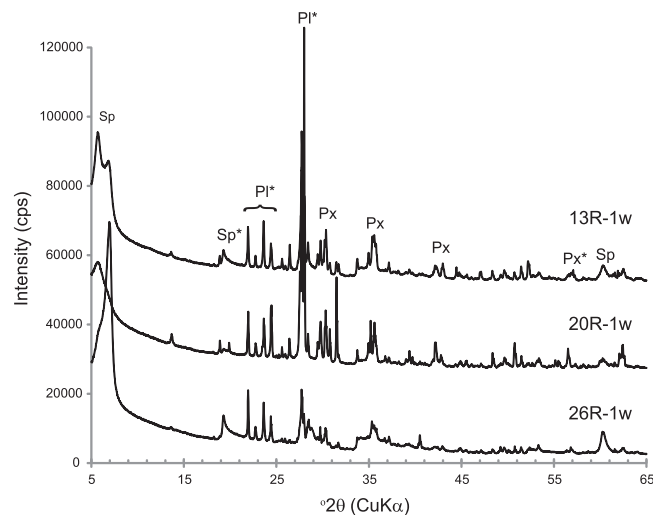


**Figure 8.** Bulk powder XRD patterns for upper pillow (13R-1w), massive basalt (20R-1w) and lower pillow basalt (26R-1w). Sp=saponite; PI=plagioclase; Px=pyroxene. Peaks marked by stars are reflections for quantitative analyses.

$$\Gamma > (k \rho g) / L \mu, \quad (6)$$

where  $\Gamma$  is the volumetric magnitude of the source ( $V_{\text{fluid}} V_{\text{sediment}}^{-1} \text{ s}^{-1}$ ),  $k$  is permeability,  $\rho$  is fluid density,  $g$  is gravity,  $L$  is the characteristic path length, and  $\mu$  is dynamic viscosity. We quantify this relationship using the permeability-porosity relationship developed by *Spinelli et al.* [2006] in which  $\log_{10}(k) = -21.33 + 6.89\phi$ . Fluid density and viscosity are varied as a function of temperature [*Huyakorn and Pinder, 1977; Smith and Chapman, 1983*]. At the trench  $L$  is set to 25 m, half the hemipelagic unit thickness. Using a small number for  $L$  is conservative because it maximizes the right-hand-side of equation (6). We envision that fluid travels up to and then along the higher permeability decollement or through fractures in the upper plate [e.g., *Hensen et al., 2004; Sahling et al., 2008*]. An additional wrinkle is that this area hosts subduction of large bathymetric features [*von Huene et al., 2000*]. These bathymetric features are likely associated with large permeabilities characteristic of oceanic basement and may drain hemipelagic fluids. Nevertheless we feel a characteristic path length of 25 m or less as compaction progresses is a reasonable estimate. Regions of overpressures are predicted to lie between approximately 10 and 60 km landward of the trench (Figure 11d). Given the heterogeneity introduced by the subducted bathymetry our predicted overpressures are likely a maximum estimate.

## 7. Discussion

### 7.1. Comparison Between the Incoming Sediment Compositions at the CRISP Trench to Those off the Nicoya Peninsula

*Spinelli and Underwood* [2004] examined the bulk-sediment mineralogy of several shallow cores offshore of the Nicoya Peninsula, and reported that the hemipelagic mud unit contains on average only ~10 wt.% of opal but includes higher amounts of clays (~70 wt.%) than the samples from Hole

**Table 4.** Results of Quantitative Analyses on Basalt Samples

Sample	mbsf	Unit	Integrated Peak Intensity			Wt%		
			Saponite	Plagioclase	Pyroxene	Saponite	Plagioclase	Pyroxene
12R-1w-69-74	99.69	III	2038	7962	1387	18.7	63.3	18.0
13R-1w-39-44	103.99	III	3209	5883	1526	27.1	51.5	21.4
14R-3w-85-90	112.33	III	2364	6848	1766	20.7	55.6	23.8
15R-1w-68-75	113.88	III	3439	5240	849	32.8	54.5	12.7
15R-2w-35-40	115.01	III	2652	6540	1428	23.4	56.6	20.0
16R-3w-52-57	121.69	III	2899	7946	1147	23.5	62.6	13.9
18R-1w-107-111	128.87	V	1507	8311	1907	14.9	61.3	23.8
20R-1w-104-108	138.44	VI	1399	7024	1550	15.7	61.5	22.8
21R-1w-68-73	142.58	VI	1279	6392	1619	15.4	59.2	25.4
22R-1w-59-63	147.49	VI	2375	5851	1722	22.1	52.3	25.6
24R-1w-32-36	153.82	VI	3069	8752	1239	23.0	63.2	13.8
26R-1w-130-135	162.4	VIII	5191	5056	711	47.1	52.9	0.0
26R-3w-32-36	164.21	VIII	4163	4659	890	38.4	48.6	13.1
Average <sup>a</sup>						24.8 (9.1)	57.1 (4.8)	18.0 (7.0)

<sup>a</sup>Values in brackets are  $1\sigma$ .

U1381A. Because we did not independently quantify the amorphous fraction by alkali leaching method as *Spinelli and Underwood* [2004], our mineralogical data include larger uncertainty with respect to the opal content. However, the difference by up to 20 wt.% of constituents likely reflects real mineralogical changes along strike between the two areas. This mineralogical variation is most clearly exemplified in the pelagic unit. Offshore the Nicoya Peninsula, the calcareous ooze comprises the lower pelagic unit, and the interval is mostly composed of calcite (~90 wt.%) with trace amounts of opal and clays [*Spinelli and Underwood*, 2004]. This sediment composition is markedly different from those at the CRISP margin, where the pelagic unit contains abundant amorphous substances (on average ~50 wt.%; Figure 5) and may be related to higher primal productivity of siliceous planktons as well as supply of volcanic glasses probably from Galapagos hotspot volcanism.

The composition of sediments offshore the Nicoya Peninsula leads to an estimated fluid flux of 22.8 m<sup>2</sup>/yr [*Spinelli and Underwood*, 2004; *Spinelli et al.*, 2006]. Their value is substantially larger than our estimate of 6.9 m<sup>2</sup>/yr. However, on a per meter basis the results agree to within about 6% indicating that the difference in fluid flux may mostly due to the change in sediment thickness. Offshore the Nicoya Peninsula the sediment thickness varies between approximately 600 and 0 m with a median value of about 350 m derived from 3000 km of seismic reflection surveys [*Spinelli and Underwood*, 2004]. Along seismic line BGR99-7 through the CRISP drilling transect the sediment thickness is approximately 100 m but thins to the south-east over the Cocos Ridge and dramatically thickens to the northwest. For our calculations we use a sediment thickness of 100 m. This similarity in fluid flux on a per meter basis results from the fact that the fluid flux is dominated by fluids in the pore space and that the average porosity of sediments at the trench offshore the Nicoya and Osa Peninsulas are similar. Thus knowing the along strike sediment thickness at the trench would lead to reasonable estimates of fluid influx.

## 7.2. Dewatering From the Subducting Cocos Plate and Upward Fluid Migration

Our models show that peak dehydration occurs at temperatures of approximately 100°C, and correspond to landward distances from the trench of approximately 40, 30 and 15 km for the cool, warm, and hot thermal models, respectively (Figure 11d). Our modeling predicts that overpressures in the sediments are possible for landward distances between approximately 5 and 70 km. This region overlaps with the region of negative-polarity plate boundary reflections imaged by *Ranero et al.* [2008], but extends further down dip.

Numerous mud mounds and venting sites on the trench slope of the Costa Rica margin suggest active fluid venting [*Hensen et al.*, 2004; *Sahling et al.*, 2008; *Kluesner et al.*, 2013]. At CRISP drilling sites, upward fluid migration through the overriding plate is inferred from shipboard geochemical data in the recovered cores through low salinity, depletion of Cl, Mg, K and Na, and enrichment in higher chain hydrocarbons [*Vannucchi et al.*, 2012]. Thermal models [*Harris et al.*, 2010] predict temperatures too low to drive in-situ diagenetic dehydration or the thermal decomposition of organic materials within the depth of the drill holes. Observed geochemical trends are explained by ascent of dehydrated fluids from depth [*Vannucchi et al.*, 2012].

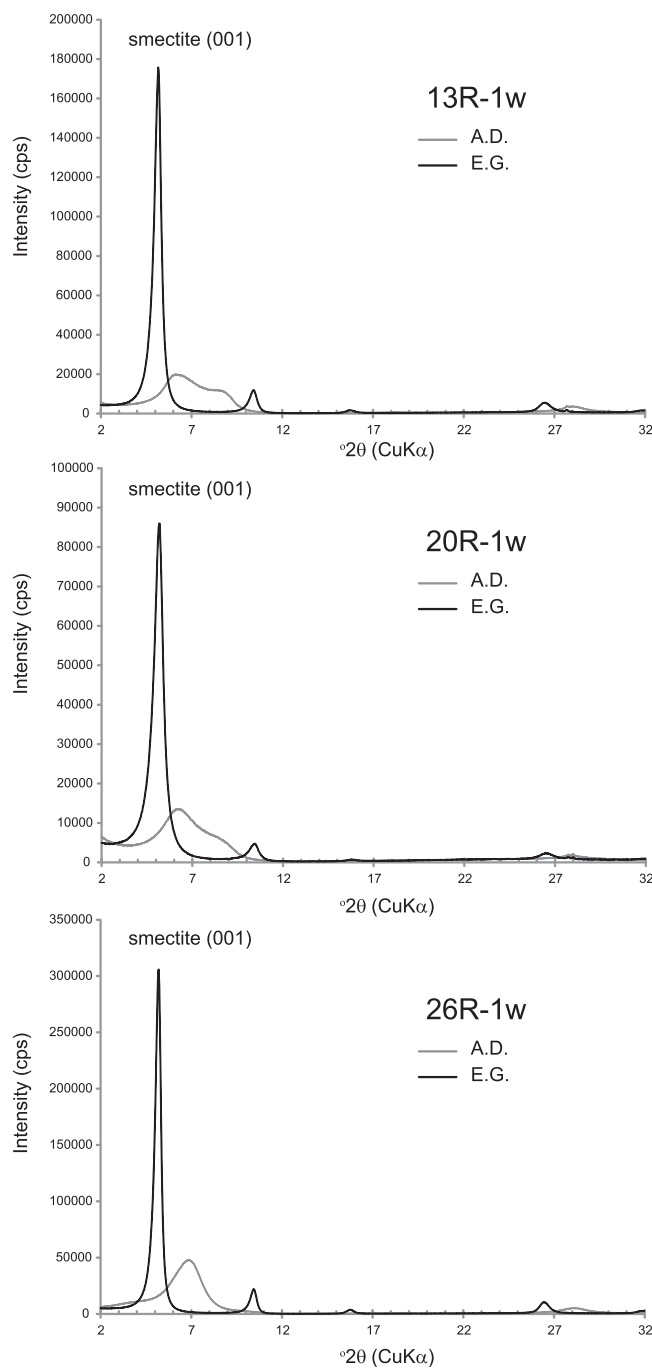


**Figure 9.** Clay-fraction XRD patterns (AD and EG states) for oriented mounts of upper pillow (13R-1w), massive basalt (20R-1w) and lower pillow basalt (26R-1w). Complex 001 peak shape in AD state reflects variable hydration states at smectite interlayer.

temperature, dehydration, and seismicity. The temperature associated with the updip onset of seismicity for cool, warm, and hot models are 70°, 90°, and 150°C, respectively (Figure 11a). We note that the difference in location between the 70° and 90° isotherm with the updip onset of seismicity is not well resolved by the thermal models [Harris et al., 2010] but is significantly different from the 150°C isotherm. Hyndman and Wang [1993] speculated that the updip limit of seismicity is well correlated with temperatures in the range of 100° to 150°C, a finding supported by thermal models at accretionary margins [Oleskevich et al., 1999], although the causative process remains enigmatic.

As shown in Figure 11, most of subsurface fluid near the trench is derived from sediment compaction, but mineral dehydration becomes significant beyond ~30 km (temperature higher than ~100°C) [Harris et al., 2010]. Moreover, the subducting basement may also act as a fluid source due to mafic clay mineral diagenesis [Kameda et al., 2011]. Although the permeability would likely be too high to support overpressures, saponite commonly observed in the basement samples may also contribute to hydrologic processes by chloritization reaction. Future analyses of trace elements and isotopes of volatile components will provide further constraints on the origin, temperature and mixing process of deep sourced fluids at the CRISP margin.

### 7.3. Implication to Interplate Seismicity Along the CRISP Transect

It is instructive to compare this potential overpressure region with the observed seismogenic zone. DeShon et al. [2003] relocated approximately 300 aftershocks resulting from the  $M_w$  6.9, 20 August 1999, Quepos, Costa Rica earthquake. They used these aftershocks to define the seismogenic zone and found it to be between 30 and 95 km landward of the trench. Arroyo et al. [2014] analyzed the  $M_w$  6.4, 16 June 2002, Osa, Costa Rica earthquake and its aftershocks. They found that the main shock likely occurred along the plate interface, 25 km landward of the trench at a depth of approximately 5–10 km. Both studies were aided with a local ocean bottom seismic network and a nearby land seismic network.

The thermal models explored in this study lead to distinctly different implications for the relationship between

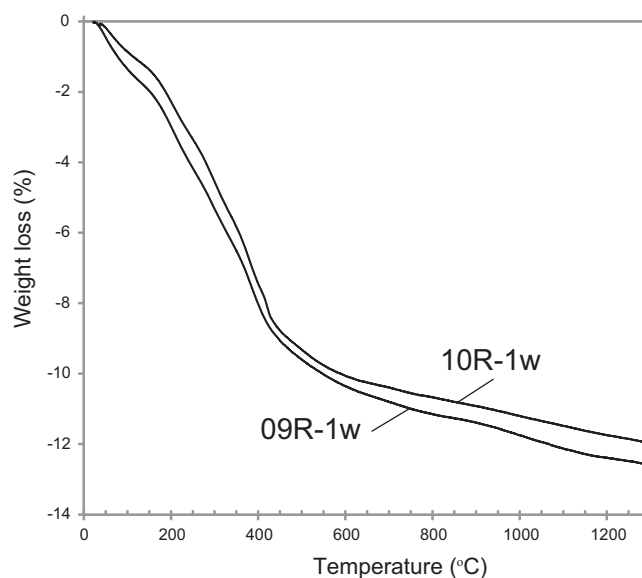


**Figure 10.** Weight loss during Thermogravimetric and differential thermal analysis (TG-DTA) for purified biogenic silica in pelagic ooze samples. The profiles suggest that water content in these samples is ~12 wt%.

A leading hypothesis for the relationship between temperature and the updip limit of seismicity is that waning fluid generation leads to diminished pore pressures and larger effective stress [Moore and Saffer, 2001]. The cool and warm models predict peak mineralogic fluid release landward of the updip onset of seismicity. In contrast the hot model predicts peak mineralogic fluid release seaward of the updip onset of seismicity.

We discount the hot model following two lines of evidence. First, temperatures on the plate boundary are estimated based on extrapolating surface values of heat flow to the plate interface. This process neglects the cooling effect of plate convergence. Offshore the CRISP transect plate convergence is fast at a rate of 8.5 cm/yr so that the cooling effect is relatively large. Second,

Hensen et al. [2004] find fluids indicative of clay-mineral dehydration reactions at mounds 11 and 12, just northwest of the CRISP drilling transect. These mounds are ~35 km landward of the trench axis, a position where the hot model predicts temperatures in excess of 150°C such that clay dehydration is mostly complete. Geochemical evidence including Cl depletion, B enrichment, and relationships between  $\delta^{18}\text{O}$  and  $\delta\text{D}$  indicate that the fluids are the result of dehydration products from sediments on the subducting plate and that the fluids formed at temperatures no higher than 130°C [Hensen et al., 2004]. These results suggest that clay dehydration is occurring in significant quantities at least 35 km landward of the trench.

Here we argue that the updip limit of seismicity as defined by DeShon et al. [2003] and Arroyo et al. [2014] has a different relationship with temperature at this margin than observed at accretionary margins. Accretionary margins are typified by thick sequences of incoming sediment. To accrete sediments the plate boundary cuts down into the typically clay rich and low permeability sediment. In contrast plate boundaries at erosive margins form at the top of the incoming sediment in the nonaccretionary mode or cut up into the overriding plate in the erosive mode [von Huene and Scholl, 1991].

In the CRISP drilling region shallow seismicity is correlated with the subduction of bathymetric relief [Husen et al., 2003; Bilek et al., 2003; DeShon et al., 2003]. Bilek et al. [2003] point out that seismicity in this area occur in patches elongated downdip with patch widths matching the width of incoming bathymetric features such as the Quepos Plateau. Further, bathymetric highs in this area are capped by velocity-weakening nannofossil chalk [Ikari et al., 2013]. We envision the plate boundary as a corrugated surface in

which bathymetric highs capped with nannofossil chalk form the peaks and hemipelagics and pelagics infill the troughs. If the bathymetric highs act as indentors thereby facilitating the process of subduction erosion, the plate boundary must pass over the seamounts and may pass through the nannofossil chalk. Because nannofossil chalk is not a hydrous mineral it would not generate overpressures through dehydration and subduction erosion

**Table 5.** Fluid Influx Rate ( $\text{m}^3/\text{yr}$ ) for Each Unit

Unit and Lithology	Thickness (m)	Host	Wt. % solid	Vol % Bulk	Fluid Influx Rate ( $\text{m}^2/\text{yr}$ )
I Hemipelagic	50	Opal	30	8.4	$8.4 \times 10^{-2}$
I Hemipelagic		Smectite	50	12.1	0.20
I Hemipelagic		Pore		75	3.19
II Pelagic	50	Opal	53	13	0.13
II Pelagic		Pore		78	3.32
Basement	70	Saponite	25	24	$0.54 (4.0^a \times 10^{-3})$
Basement		Pore		5	0.30
Total					7.5

<sup>a</sup>Volume of influx water ( $\text{m}^3$ ) per unit thickness of solid.

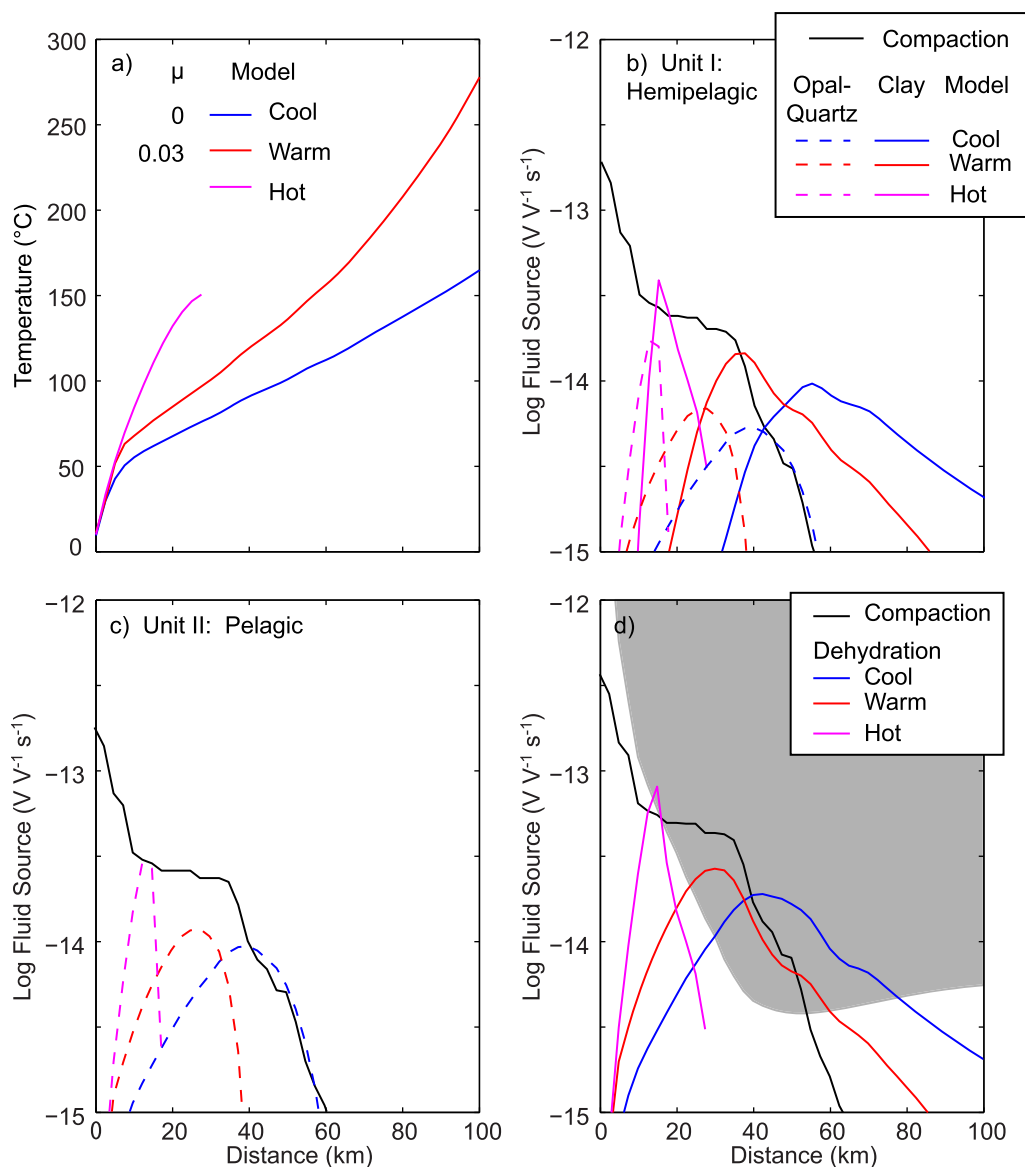


**Figure 11.** Thermal models and fluid release along the CRISP transect. (a) Sediment temperature as a function of landward distance from the trench. Cool and warm models from *Harris et al.* [2010], hot model from *Ranero et al.* [2008].  $\mu$  is the coefficient of friction. (b) Fluid release in the hemipelagic unit. (c) Fluid release in the pelagic unit, same symbols as in Figure 11b. (d) Fluid release from compaction and mineral dehydration. Shaded region shows area of potential sediment overpressures.

would enhance permeability. These processes may yield frictional instabilities independent of temperature. In this way the aseismic/seismic transition associated with bathymetric highs could occur updip of modeled peak clay and opal-quartz dehydration and at lower temperatures than observed elsewhere [e.g., *Oleskevich et al.*, 1999]. In contrast, bathymetric lows are infilled with velocity-strengthening hemipelagic material [*Ikari et al.*, 2013; *Namiki et al.*, 2014]. *Namiki et al.* [2014] examined frictional properties of hemipelagic and pelagic samples from Site U1380. They showed that the hemipelagic clays have consistently lower friction coefficient values ( $\sim 0.2$ ) than the pelagic ooze samples (0.6–0.8). This difference is likely due to the higher smectite content in the hemipelagic samples. In our view, the hemipelagic layer may host the décollement between the bathymetric highs and these regions would likely show a relationship between temperature and the updip limit of seismicity through dehydration reactions. We suggest that at the shallowest levels of observed seismicity, alternating regions of velocity weakening chalk capped bathymetric highs alternate with velocity strengthening dehydrating hemipelagics that infill bathymetric lows. This alternation in frictional properties generates the observed patchiness of seismicity.

Our results emphasize the importance of frictional heterogeneities along the subduction thrust [Bilek *et al.*, 2003] due to bathymetric relief in some areas and overpressured hemipelagics in others. Globally, this heterogeneity may be more pronounced at erosive convergent margins where the incoming sediment thickness is small relative to the size of bathymetric relief.

## 8. Conclusions

On the basis of this study we conclude the following:

1. The mineral composition of sediments and saponite-bearing oceanic crust quantified by XRD indicates that incoming materials contain considerable amounts of hydrous phases. These phases include dioctahedral smectite and biogenic silica in the sediment and saponite in the basement. The total influx of sedimentary water at the CRISP margin is  $6.9 \text{ m}^2/\text{yr}$  per meter of along strike. This quantity of water is smaller than that offshore the Nicoya Peninsula due to the thinner incoming sediments at the CRISP drilling transect.
2. Dehydration of the hydrous phases within the hemipelagics predicted from cool and warm thermal models for the subduction zone act peaks between approximately 30 and 40 km landward of the trench. This fluid is the main source of fresh water released at depth. Dehydration from hydrous phases predicted by the hot thermal model peaks at approximately 15 km landward of the trench and appears inconsistent with the geochemistry of fluids from seeps. The upward migration of low-salinity water may account for geochemical signatures observed in trench slope cores recovered along the CRISP transect.
3. Modeling of dewatering by sediment compaction and silica/clay dehydrations suggests that these processes can potentially generate fluid overpressure within the subducting sediment layer at distances of approximately 5 and 70 km landward of the trench.
4. Peak mineralogic dehydration occurs seaward of shallow seismicity for our warm and cool models. We suggest that this observation is additional evidence that shallow seismicity is associated with bathymetric highs that juxtapose oceanic basement with the upper plate and illustrates the importance of heterogeneity in the frictional properties of the subduction thrust.

## Acknowledgments

This research used samples and data provided by Integrated Ocean Drilling Program. This work was supported by Grants-in-Aid from JSPS for Young Scientists (24740339) and from MEXT for Scientific Research on Innovative Areas (21107005) and to Harris by the National Science Foundation through the U.S. Science Support Program for IODP that is administered by the Consortium for Ocean Leadership. We thank two anonymous reviewers and G. Spinelli and R. Lauer for useful discussions during the revision of this manuscript.

## References

- Arroyo, I. G., I. Grevenmeyer, C. R. Ranero, and R. von Huene (2014), Interplate seismicity at the CRISP drilling site: The 2002 Mw 6.4 Osa Earthquake at the southeastern end of the Middle America Trench, *Geochem. Geophys. Geosyst.*, *15*, 3035–3050, doi:10.1002/2014GC005359.
- Bilek, S. L., S. Y. Schwartz, and H. R. DeShon (2003), Control of seafloor roughness on earthquake rupture behavior, *Geology*, *31*, 455–458, doi:10.1130/0091-7613(2003)031<0455:COSROE>2.0.CO;2.
- Bird, P. (1984), Hydration-phase diagrams and friction of montmorillonite under laboratory and geologic conditions, with implications for shale compaction, slope stability, and strength of fault gouge, *Tectonophysics*, *107*, 235–60.
- Biscaye, P. E. (1965), Mineralogy and sedimentation of recent deep-sea clays in the Atlantic Ocean and adjacent seas and oceans, *Geol. Soc. Am. Bull.*, *76*, 803–832.
- Bray, C. J., and D. E. Karig (1985), Porosity of sediments in accretionary prisms and some implications for dewatering processes, *J. Geophys. Res.*, *90*(B1), 768–778.
- Cann, J. R., and R. P. von Herzen (1983), Downhole logging at Deep Sea Drilling Project sites 501, 504, and 505, near the Costa Rica Rift, *Deep Sea Drill. Proj. Initial Rep.*, *69*, 281–299.
- DeMets, C. (2001), A new estimate for present-day Cocos-Caribbean plate motion: Implications for slip along the Central American Volcanic Arc, *Geophys. Res. Lett.*, *28*, 4043–4046, doi:10.1029/2001GL013518.
- DeShon, H. R., S. Y. Schwartz, S. L. Bilek, L. M. Dorman, V. Gonzalez, J. M. Protti, E. R. Flueh, and T.H., Dixon (2003), Seismogenic zone structure of the southern Middle America Trench, Costa Rica, *J. Geophys. Res.*, *108*(B10), 2491, doi:10.1029/2002JB002294.
- Dixon, T.H. (2003), Relations between seismic coupling and mountain building based on GPS observations in Costa Rica, *Geophys. Res. Abstr.*, *5*, 04374.
- Fisher, A. T., and M. B. Underwood (1995), Calibration of an X-ray diffraction method to determine relative mineral abundance in bulk powders using matrix singular value decomposition: A test from the barbados accretionary complex, in *Proceedings of Ocean Drilling Program Initial Reports 156*, edited by T. H. Shipley *et al.*, pp. 29–37, Ocean Drilling Program, College Station, Tex.
- Fitts T. G., and K. M. Brown (1999), Stress-induced smectite dehydration: Ramifications for patterns of freshening and fluid expulsion in the N. Barbados accretionary wedge, *Earth Planet. Sci. Lett.*, *172*, 179–197.
- Garcia-Valles, M., J. L. Fernandez-Turiel, D. Gimeno-Torrente, J. Saavedra-Alonso, and S. Martinez-Manent (2008), Mineralogical characterization of silica sinters from the El Tatío geothermal field, Chile, *Am. Mineral.*, *93*, 1373–1383.
- Hacker, B. R. (2008), H<sub>2</sub>O subduction beyond arcs, *Geochem. Geophys. Geosyst.*, *9*, Q03001, doi:10.1029/2007GC001707.
- Harris, R. N., G. Spinelli, C. R. Ranero, I. Grevenmeyer, H. Villinger, and U. Barckhausen (2010), Thermal regime of the Costa Rican convergent margin: 2. Thermal models of the shallow Middle America subduction zone offshore Costa Rica, *Geochem. Geophys. Geosyst.*, *11*, Q12529, doi:10.1029/2010GC003273.

- Hensen, C., K. Wallmann, M. Schmidt, C. R. Ranero, and F. Suess (2004), Fluid expulsion related to mud extrusion off Costa Rica—A window to the subducting slab, *Geology*, *32*(3), 201–204, doi:10.1130/G20119.1.
- Hey, R. (1977), Tectonic evolution of the Cocos-Nazca spreading center, *Geol. Soc. Am. Bull.*, *88*, 1404–1420. doi:10.1130/0016-7606(1977)88<i>:TEOTCS>2.0.CO;2.
- Husen, S., R. Quintero, E. Kissling, and B. Hacker (2003), Subduction zone structure and magmatic processes beneath Costa Rica constrained by local earthquake tomography and petrological modelling, *Geophys. J. Int.*, *155*, 11–32.
- Huyakorn, P. S., and G. F. Pinder (1977), A pressure-enthalpy finite element model for simulating hydrothermal reservoirs, paper presented at Second International Symposium on Computer Methods for Partial Differential Equations, Lehigh Univ., Bethlehem, Penn.
- Hyndman, R. D., and K. Wang (1993), Thermal constraints on the zone of major thrust earthquake failure: The Cascadia subduction zone, *J. Geophys. Res.*, *98*(B2), 2039–2060.
- Ikari, M. J., A. R. Niemeijer, C. J. Spiers, A. J. Kopf and D. M. Saffer (2013), Experimental evidence linking slip instability with seafloor lithology and topography at the Costa Rica convergent margin, *Geology*, *41*, 891–894.
- Inoue, A., A. Bouchet, B. Velde, and A. Meunier (1989), Convenient technique for estimating smectite layer percentage in randomly interstratified illite/smectite minerals. *Clays Clay Miner.*, *37*, 227–234.
- Kameda, J., A. Yamaguchi, S. Saito, H. Sakuma, K. Kawamura, and G. Kimura (2011), A new source of water in seismogenic subduction zones, *Geophys. Res. Lett.*, *38*, L22306, doi:10.1029/2011GL048883.
- Kastner, M. (1981), Authigenic silicates in deep-sea sediments: Formation and diagenesis, in *The Sea*, vol. 7, edited by C. Emiliani, pp. 915–80, Wiley-Interscience, N. Y.
- Kastner, M., H. Elderfield, and J. B. Martin (1991), Fluids in convergent margins: What do we know about their composition, origin, role in diagenesis and importance for oceanic chemical fluxes?, *Philos. Trans. R. Soc. London A*, *335*, 243–59.
- Kastner, M., E. Solomon, R. Harris, and M. Torres (2014), Fluid origins, thermal regimes, and fluid and solute fluxes in the forearc of subduction zones, in *Earth and Life Processes Discovered Beneath the Seafloor*, edited by R. Stein et al., pp. 671–734, Elsevier, doi:10.1016/B978-0-444-62617-2.00022-0.
- Kluesner, J. W., E. A. Silver, N. L. Bangs, K. D. McIntosh, J. Gibson, D. Orange, C. R. Ranero, and R. Huene (2013), High density of structurally controlled, shallow to deep water fluid seep indicators imaged offshore Costa Rica, *Geochem. Geophys. Geosyst.*, *14*, 519–539. doi:10.1002/ggge.20058.
- Lonsdale, P., and K. D. Klitgord (1978), Structure and tectonic history of the eastern Panama Basin, *Geol. Soc. Am. Bull.*, *89*, 981–999. doi:10.1130/0016-7606(1978)89<981:SATHOT>2.0.CO;2.
- Mizutani, S. (1977), Progressive ordering of cristobalitic silica in the early stage of diagenesis, *Contrib. Mineral. Petrol.*, *64*, 129–140.
- Molnar, P., and P. England (1995), Temperatures in zones of steady-state underthrusting of young oceanic lithosphere, *Earth Planet. Sci. Lett.*, *131*, 57–70.
- Moore, J. C., and D. M. Saffer (2001), Updip limit of the seismogenic zone beneath the accretionary prism of southwest Japan: An effect of diagenetic to low-grade metamorphic processes and increasing effective stress, *Geology*, *29*, 183–186.
- Moore, J. C., and P. Vrolijk (1992), Fluids in accretionary prisms, *Rev. Geophys.*, *30*(2), 113–135, doi:10.1029/92RG00201.
- Namiki, Y., A. Tsutsumi, K. Ujiie, and J. Kameda (2014), Frictional properties of sediments entering the Costa Rica subduction zone offshore the Osa Peninsula: Implications for fault slip in shallow subduction zones, *Earth Planets Space*, *66*:72, doi:10.1186/1880-5981-66-72.
- Neuzil, C. E. (1995), Abnormal pressures as hydrodynamic phenomena, *Am. J. Sci.*, *295*, 742–786.
- Oleskevich, D., R. Hyndman, and K. Wang (1999), The updip and downdip limits to great subduction earthquakes: Thermal and structural models of Cascadia, south Alaska, SW Japan, and Chile, *J. Geophys. Res.*, *104*(B7), 14,965–14,991.
- Peacock, S. M. (1990), Fluid processes in subduction zones, *Science*, *248*, 329–337.
- Pytte, A. M., and R. C. Reynolds (1989), The thermal transformation of smectite to illite, in *The Thermal History of Sedimentary Basins*, edited by N. D. Naeser and T. H. McCulloh, pp. 133–140, Springer, N. Y.
- Ranero, C. R., and R. von Huene (2000), Subduction erosion along the Middle America convergent margin, *Nature*, *404*, 748–752, doi:10.1038/35008046.
- Ranero, C. R., R. von Huene, E. Flueh, M. Duarte, D. Baca, and K. McIntosh (2000), A cross section of the convergent Pacific margin of Nicaragua, *Tectonics*, *19*, 335–357, doi:10.1029/1999TC900045.
- Ranero, C. R., I. Grevemeyer, U. Sahling, U. Barckhausen, C. Hensen, K. Wallmann, W. Weinrebe, P. Vannucchi, R. von Huene, and K. McIntosh (2008), Hydrogeological system of erosional convergent margins and its influence on tectonics and interplate seismogenesis, *Geochem. Geophys. Geosyst.*, *9*, Q03S04, doi:10.1029/2007GC001679.
- Saffer, D. M., and H. J. Tobin (2011), Hydrogeology and mechanics of subduction zone forearcs: Fluid flow and pore pressure, *Annu. Rev. Earth Planet. Sci.*, *39*, 157–186.
- Saffer, D. M., M. B. Underwood, and A. W. McKiernan (2008), Evaluation of factors controlling smectite transformation and fluid production in subduction zones: Application to the Nankai Trough, *Island Arc*, *17*, 208–230, doi:10.1111/j.1440-1738.2008.00614.x.
- Sahling, H., D. G. Masson, C. R. Ranero, V. Hühnerbach, W. Weinrebe, I. Klauke, D. Bürk, W. Brückmann, and E. Suess (2008), Fluid seepage at the continental margin offshore Costa Rica and southern Nicaragua, *Geochem. Geophys. Geosyst.*, *9*, Q05S05, doi:10.1029/2008GC001978.
- Sandford, F. (2003), Physical and chemical analysis of the siliceous skeletons in six sponges of two groups (Demospongiae and Hexactinellida), *Microsc. Res. Tech.*, *62*, 336–355, doi:10.1002/jemt.10400.
- Schmidt, M., C. Hensen, T. Mörz, C. Müller, I. Grevemeyer, K. Wallmann, S. Mau, and N. Kaul (2005), Methane hydrate accumulation in “Mound 11” mud volcano, Costa Rica forearc, *Mar. Geol.*, *216*, 83–100.
- Shipboard Scientific Party (1997a), Site1039, Proc. Ocean Drill. Progr. Init. Rep. 170, 45–93.
- Shipboard Scientific Party (1997b), Site1040, Proc. Ocean Drill. Progr. Init. Rep. 170, 95–152.
- Shipboard Scientific Party (1997c), Site1041, Proc. Ocean Drill. Progr. Init. Rep. 170, 153–188.
- Smith, L., and D. S. Chapman (1983), On the thermal effects of groundwater flow: 1. Regional scale systems, *J. Geophys. Res.*, *88*(B1), 593–608.
- Spinelli, G., and K. Wang (2009), Links between fluid circulation, temperature, and metamorphism in subducting slabs, *Geophys. Res. Lett.*, *36*, L13302, doi:10.1029/2009GL038706.
- Spinelli, G. A., and D. M. Saffer (2004), Along-strike variations in underthrust sediment dewatering on the Nicoya margin, Costa Rica related to the updip limit of seismicity, *Geophys. Res. Lett.*, *L04613*, doi:10.1029/2003GL018863.
- Spinelli, G. A., and M. B. Underwood (2004), Character of sediments entering the Costa Rica subduction zone: Implication for partitioning of water along the plate interface, *Island Arc*, *13*, 432–451.
- Spinelli, G. A., D. M. Saffer, and M. B. Underwood (2006), Hydrologic responses to three-dimensional temperature variability, Costa Rica subduction margin, *J. Geophys. Res.*, *111*, B04403, doi:10.1029/2004JB003436.

- Sutter, F. R. (1985), Sección geológica del Pacífico al Atlántico a través de Costa Rica, *Rev. Geol. Am. Cent.*, 2, 23–32. [Available at [http://www.geologia.ucr.ac.cr/revista/to\\_pdf/revista/02/02-RIVIER.pdf](http://www.geologia.ucr.ac.cr/revista/to_pdf/revista/02/02-RIVIER.pdf).]
- Vannucchi, P., D. W. Scholl, M. Meschede, and K. McDougall-Reid (2001), Tectonic erosion and consequent collapse of the Pacific margin of Costa Rica: Combined implications from ODP Leg 170, seismic offshore data, and regional geology of the Nicoya Peninsula, *Tectonics*, 20(5), 649–668, doi:10.1029/2000TC001223.
- Vannucchi, P., C. R. Ranero, S. Galeotti, S. M. Straub, D. W. Scholl, and K. McDougall-Ried (2003), Fast rates of subduction erosion along the Costa Rica Pacific margin: Implications for nonsteady rates of crustal recycling at subduction zones, *J. Geophys. Res.*, 108(B11), 2511, doi:10.1029/2002JB002207.
- Vannucchi, P., S. Galeotti, P. D. Clift, C. R. Ranero, and R. von Huene (2004), Long-term subduction-erosion along the Guatemalan margin of the Middle America Trench, *Geology*, 32, 617–620, doi:10.1130/G20422.1.
- Vannucchi, P., K. Ujije, N. Stroncik, and the Expedition 334 Scientists (2012), *Proceedings of the Integrated Ocean Drilling Program 334*, Integrated Ocean Drilling Program Manage. Int. Inc., Tokyo, doi:10.2204/iodp.proc.334.2012.
- Vannucchi, P., et al. (2013), Rapid pulses of uplift, subsidence, and subduction erosion offshore Central America: Implications for building the rock record of convergent margins, *Geology*, 41, 995–998.
- von Huene, R., and D. W. Scholl (1991), Observations at convergent margins concerning sediment subduction, subduction erosion, and the growth of continental crust, *Rev. Geophys.*, 29(3), 279–316.
- von Huene, R., et al. (2000), Quaternary convergent margin tectonics of Costa Rica, segmentation of the Cocos Plate, and Central American volcanism, *Tectonics*, 19(2), 314–334.
- Von Huene, R., C. R. Ranero, and P. Vannucchi (2004), Generic model of subduction erosion, *Geology*, 32, 913.
- Wallace, P. J. (2005), Volatiles in subduction zone magmas: Concentrations and fluxes based on melt inclusion and volcanic gas data, *J. Volcanol. Geotherm. Res.*, 140, 217–240.